coatings

MDPI

Article

Effects of Nitrogen Flow Ratio on Structures, Bonding Characteristics, and Mechanical Properties of ZrN_x Films

Yi-En Ke [1] and Yung-I Chen [1,2,*]

[1] Department of Optoelectronics and Materials Technology, National Taiwan Ocean University, Keelung 20224, Taiwan; 10889027@mail.ntou.edu.tw
[2] Center of Excellence for Ocean Engineering, National Taiwan Ocean University, Keelung 20224, Taiwan
* Correspondence: yichen@mail.ntou.edu.tw; Tel.: +886-2-2462-2192

Received: 11 April 2020; Accepted: 12 May 2020; Published: 14 May 2020

Abstract: ZrN_x (x = 0.67–1.38) films were fabricated through direct current magnetron sputtering by a varying nitrogen flow ratio [N_2/(Ar + N_2)] ranging from 0.4 to 1.0. The structural variation, bonding characteristics, and mechanical properties of the ZrN_x films were investigated. The results indicated that the structure of the films prepared using a nitrogen flow ratio of 0.4 exhibited a crystalline cubic ZrN phase. The phase gradually changed to a mixture of crystalline ZrN and orthorhombic Zr_3N_4 followed by a Zr_3N_4 dominant phase as the N_2 flow ratio increased up to >0.5 and >0.85, respectively. The bonding characteristics of the ZrN_x films comprising Zr–N bonds of ZrN and Zr_3N_4 compounds were examined by X-ray photoelectron spectroscopy and were well correlated with the structural variation. With the formation of orthorhombic Zr_3N_4, the nanoindentation hardness and Young's modulus levels of the ZrN_x (x = 0.92–1.38) films exhibited insignificant variations ranging from 18.3 to 19.0 GPa and from 210 to 234 GPa, respectively.

Keywords: bonding characteristics; mechanical properties; sputtering

1. Introduction

Multifunctional ZrN films have been extensively investigated due to their characteristics including golden yellow appearance [1–3], high hardness [3–6], corrosion resistance [7–9], and wear resistance [10]. The nitrogen flow rate in reactive sputtering affects the structure and composition of fabricated MeN_x (Me = Ti, Zr, Hf) films [11–13], which varied the characteristics of these films. The B1 structure is a familiar structure for transition metal nitrides, in which N occupies the interstitial sites of close-packed metal atoms. Moreover, a wide composition range, with point defects in the B1 structure, was obtained for transition metal nitrides [14]. By contrast, N-rich compounds such as Ti_3N_4, Zr_3N_4, and Hf_3N_4 have been reported [15]. Zr_3N_4 crystallizes in an orthorhombic (o-Zr_3N_4) [16–18] or cubic (c-Zr_3N_4) [19–23] phase. o-Zr_3N_4 was reported as a transparent insulator [16,24], whereas c-Zr_3N_4 with a cubic Th_3P_4-type structure was suggested as an alternating hard material [19,23]. Mattesini et al., [23] reported the calculated hardness level of c-Zr_3N_4 to be 17.5–19.7 GPa. Chhowalla and Unalan [25] announced that the filtered cathodic arc fabricated c-Zr_3N_4 films stabilized by a high residual stress and showed a high hardness of 36 GPa, compared to 27 GPa for the low-stressed o-Zr_3N_4 films. Zr_3N_4 contained films fabricated through sputtering technologies that were also reported either in the o-Zr_3N_4 or the c-Zr_3N_4 forms [12,16,18,26,27]. Previous studies [12,16,28] have reported that interstitial N is incorporated into the ZrN structure to form a Zr_3N_4 phase as the nitrogen flow ratio was higher than the critical level to form stoichiometric ZrN. Takeyama et al., [18] reported that a bilayered ZrN/o-Zr_3N_4 barrier was thermally stable undergoing the annealing at 500 °C for 60 min, but the

o-Zr_3N_4 barrier was metastable in the Zr–N system. Kroll [15] proposed that c-Zr_3N_4 is obtained in a high-pressure state. Alternatively, Meng et al., [27] reported the phase transformation from ZrN to c-Zr_3N_4 under high-compressive stress by increasing the substrate bias voltage in direct current magnetron sputtering (DCMS). In a previous study [29], HfN_x films with stoichiometric variable x in the range of 0.81–2.07 were deposited through DCMS using nitrogen flow ratios of 0.1 to 1.0. The structure varied from a δ-HfN phase to a near-amorphous structure as the stoichiometric variable x increased, which was accompanied by a change in the bonding characteristics from HfN to Hf_3N_4-dominant and a decrease in mechanical properties. In this study, the influences of nitrogen flow ratio on the structural evolution, bonding characteristics, and mechanical properties of ZrN_x films fabricated through DCMS were investigated.

2. Materials and Methods

ZrN_x films were prepared on silicon substrates through reactive DCMS. Figure 1 schematically displays the related positions of sputter targets and the samples in the sputtering chamber. A sputtering gun (gun 1) with Zr target was operated at 150 W in the sputtering process using a N_2 flow ratio [$f = N_2/(Ar + N_2)$] ranging from 0.50 to 0.85 and a sputter time of 180 min. As the deposition rate decreased with increasing N_2 flow ratios (Table 1), both guns 1 and 2, with powers of 150 W, were utilized for raising the deposition rate of the process with $f = 1.00$. $Zr_{60}N_{40}$ films prepared with an N_2 flow ratio of 0.4, gun 1 power of 300 W, and sputter time of 60 min, that were reported in a previous study [30], are discussed for comparison. The diameter of Zr targets was 50.8 mm. The total flow rates of Ar and N_2 were fixed at 20 sccm with a working pressure of 0.4 Pa. The target-to-substrate distance was 90 mm. The electrically-grounded substrate holder was rotated at 5 rpm.

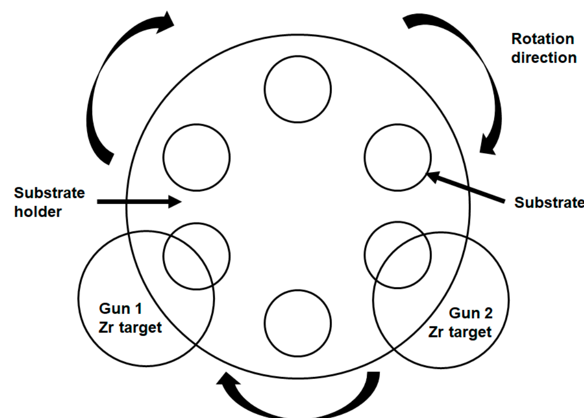

Figure 1. Relationship of sputter targets to the sample positions.

Table 1. Chemical composition and deposition rates of ZrN_x films prepared using various N_2 flow ratios.

Sample	f [a]	Chemical Composition (at.%)				x [b]	Thickness (nm)	D [c] (nm/min)
		Zr	N	Si	O			
P_1 [d] = 300 W, P_2 [e] = 0 W								
$Zr_{60}N_{40}$	0.40	57.9 ± 0.8	38.8 ± 0.8	-	3.3 ± 0.1	0.67	820	13.7
P_1 = 150 W, P_2 = 0 W								
$Zr_{52}N_{48}$	0.50	49.3 ± 0.8	46.4 ± 1.1	1.6 ± 0.0	2.5 ± 0.2	0.92	680	3.8
$Zr_{50}N_{50}$	0.65	48.0 ± 2.0	47.3 ± 2.2	1.8 ± 0.0	2.8 ± 0.3	1.00	616	3.4
$Zr_{48}N_{52}$	0.75	44.1 ± 0.4	47.8 ± 0.3	4.8 ± 0.1	3.2 ± 0.1	1.08	556	3.1
$Zr_{45}N_{55}$	0.85	39.5 ± 1.6	47.5 ± 2.2	10.8 ± 0.4	2.2 ± 0.2	1.22	348	1.9
P_1 = 150 W, P_2 = 150 W								
$Zr_{42}N_{58}$	1.00	40.5 ± 0.0	56.0 ± 0.2	1.5 ± 0.2	2.0 ± 0.1	1.38	694	3.9

[a] f: N_2 flow ratio; [b] x: stoichiometric variable; [c] D: deposition rate; [d] P_1: power on gun 1; [e] P_2: power on gun 2.

A field-emission electron probe microanalyzer (FE-EPMA, JXA-8500F, JEOL, Akishima, Japan) was used to analyze the chemical composition of the films. The thickness of films was evaluated by field emission scanning electron microscopy (FE-SEM, S4800, Hitachi, Tokyo, Japan). An X-ray diffractometer (XRD, X'Pert PRO MPD, PANalytical, Almelo, The Netherlands) with Cu Kα radiation was used to analyze the phases of the films, using the grazing incidence technique with an incidence angle of 1°. The hardness and Young's modulus values of films were measured using a nanoindentation tester (TI-900 Triboindenter, Hysitron, MN, USA) equipped with a Berkovich diamond probe tip, and were determined from 8 measurements based on the Oliver and Pharr method [31]. The indentation depth was 50 nm. The residual stress of the films measured by the curvature method was calculated using Stoney's equation [32,33],

$$\sigma_f t_f = \frac{E_S {h_S}^2}{6(1 - \nu_S) R_f} \quad (1)$$

where σ_f is the residual stress, t_f is the film thickness, E_S is the Young's modulus of Si (130.2 GPa), ν_S is Poisson's ratio for Si (0.279), h_S is the substrate thickness (525 μm), and R_f is the radius of the curvature of the sample. The chemical states of the constituent elements were examined by using an X-ray photoelectron spectroscope (XPS, PHI 1600, PHI, Kanagawa, Japan) with an Mg K*a* X-ray beam and calibrated with the C 1*s* line at 284.6 eV. The nanostructure of the samples with a protective Pt layer was observed using transmission electron microscopy (TEM, JEM-2010F, JEOL, Akishima, Japan). The average surface roughness (*Ra*) of the films determined from 3 measurements was evaluated by using an atomic force microscope (AFM, Dimension 3100 SPM, NanoScope IIIa, Veeco, Santa Barbara, CA, USA) with a scanned area of 5 μm × 5 μm [33].

3. Results

3.1. Chemical Compositions and Crystalline Phases

Table 1 lists the chemical composition of the ZrN_x films fabricated with various f values. The ZrN_x samples were named in the form $Zr_yN_{(100-y)}(f)$. The silicon contents were 1.5–1.8 at.% for the $Zr_{52}N_{48}$(0.50), $Zr_{50}N_{50}$(0.65), and $Zr_{42}N_{58}$(1.00) films with thicknesses of 616 to 694 nm, whereas the $Zr_{48}N_{52}$(0.75) and $Zr_{45}N_{55}$(0.85) films exhibited high Si contents of 4.8 and 10.8 at.%, respectively, which were attributed to lower thickness values of 556 and 348 nm. Therefore, the Si signals contributed by the Si substrates were observed. In our previous study [30], the $Zr_{60}N_{40}$(0.40) films prepared using the same sputter equipment with a sputter power of 300 W, N_2 flow ratio of 0.4, and sputter time of 60 min exhibited a thickness of 820 nm and Si-free chemical composition. The O contents of 2 to 3 at.% in the ZrN_x films were comparable with our previous study using a DCMS system [30,33]. The stoichiometric variable x increased from 0.92 to 1.00, 1.08, and 1.22 with an increasing f from 0.50 to 0.65, 0.75, and 0.85. This was accompanied by a decrease in the deposition rate from 3.8 to 3.4, 3.1, and 1.9 nm/min as only gun 1 was applied with a DC power of 150 W. The decrease in deposition rate with the increasing f level was caused by the reduced ionization and sputtering yield of N_2 related to Ar gas [34]. Moreover, the well-known target poisoning effect in reactive sputtering reduced the deposition rate [34–36]. The $Zr_{42}N_{58}$(1.00) films prepared using an f of 1.00 and sputter power of 150 W on both guns 1 and 2 exhibited an x of 1.38 and a deposition rate of 3.9 nm/min; this deposition rate was almost twice that of the $Zr_{45}N_{55}$(0.85) films prepared with a high f level and using gun 1 only.

Figure 2a shows the XRD patterns of the ZrN_x films. In a previous study [30], the XRD pattern of the $Zr_{60}N_{40}$(0.40) films exhibited a ZrN phase [ICDD 00-035-0753] with evident (111), (200), (220), (311), and (222) reflections, which are also shown in Figure 2a for comparison. Ramana et al., [35] reported that ZrN films prepared with an $f < 0.28$ through DCMS were crystalline. The stoichiometric variable x (N/Zr) increased by raising the f level either in DCMS [35] or hollow cathode discharge ion-plating [37]. The $Zr_{52}N_{48}$(0.50), $Zr_{50}N_{50}$(0.65), and $Zr_{48}N_{52}$(0.75) films exhibited a ZrN phase and an extra reflection identified as orthorhombic Zr_3N_4(320) [ICDD 00-051-0646], which was comparable with findings reported by Signore et al. [17]. The ZrN(200) reflections of the $Zr_{60}N_{40}$(0.40), $Zr_{52}N_{48}$(0.50),

$Zr_{50}N_{50}$(0.65), and $Zr_{48}N_{52}$(0.75) films exhibited lattice constants of 0.4622, 0.4653, 0.4676, and 0.4682 nm, respectively, which implied that at an angle of 2θ, the ZrN(111) reflections should be 33.58°, 33.35°, 33.18°, and 33.14°, respectively; therefore, the overlapped reflections at two-theta angle at around 32°–33° were fitted as shown in Figure 2b. The ZrN(111) reflections of the $Zr_{45}N_{55}$(0.85) and $Zr_{42}N_{58}$(1.00) films, which had no ZrN(200) reflections, were positioned at 33.14°. No Zr_3N_4 reflection was observed for the $Zr_{60}N_{40}$(0.40) films. The intensity ratio of ZrN(111):Zr_3N_4(320) varied from 54:46 to 49:51, 44:56, 37:63, and 33:67 as the f value increased from 0.50 to 0.65, 0.75, 0.85, and 1.00, which implied that the phase varied from ZrN to Zr_3N_4-dominant as the f value increased. Figure 2a shows that the insignificant reflection at 2θ ≈ 55° for $Zr_{45}N_{55}$(0.85) and $Zr_{42}N_{58}$(1.00) films could be a combination of ZrN(220), Zr_3N_4(251), Zr_3N_4(511), and Zr_3N_4(002).

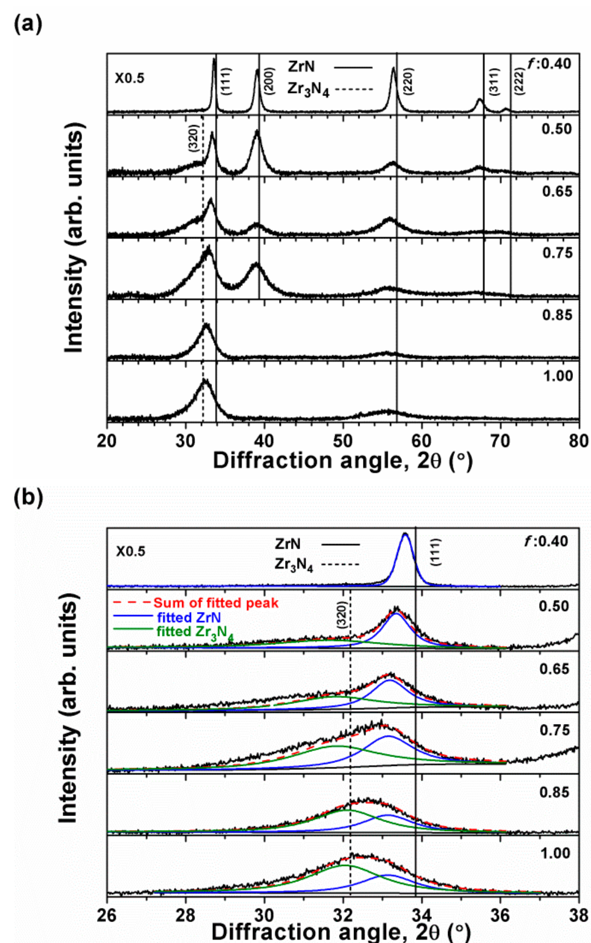

Figure 2. (**a**) and (**b**) X-ray diffraction (XRD) patterns of ZrN_x films prepared using various N_2 flow ratios (f).

Figure 3a displays the cross-sectional TEM image of $Zr_{48}N_{52}$(0.75) films, which exhibit a dense structure. The selected area diffraction pattern (SADP) at the near surface region exhibited ZrN and o-Zr_3N_4 phases. Figure 3b displays a high-resolution TEM image of $Zr_{48}N_{52}$(0.75) films, which indicates a nanocrystalline structure comprising ZrN and o-Zr_3N_4 crystallites distributed randomly. The fast Fourier transform (FFT) and lattice fringes of selected regions indicated ZrN(200) and o-Zr_3N_4(320) crystallites with d-spacings of 0.225 and 0.276 nm, respectively. Figure 4a illustrates the cross-sectional TEM image of $Zr_{42}N_{58}$(1.00) films, which SADP is a diffused ring pattern corresponding to o-Zr_3N_4. Figure 4b displays the high-resolution TEM image of $Zr_{42}N_{58}$(1.00) films, whereby only o-Zr_3N_4 crystallites are observed.

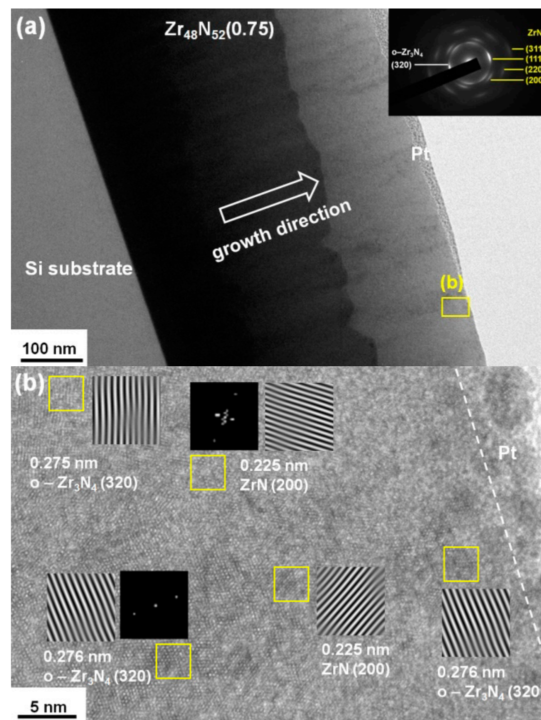

Figure 3. (**a**) Cross-sectional transmission electron microscope (TEM) image and selected area diffraction pattern (SADP), and (**b**) a high-resolution image of the $Zr_{48}N_{52}$(0.75) films.

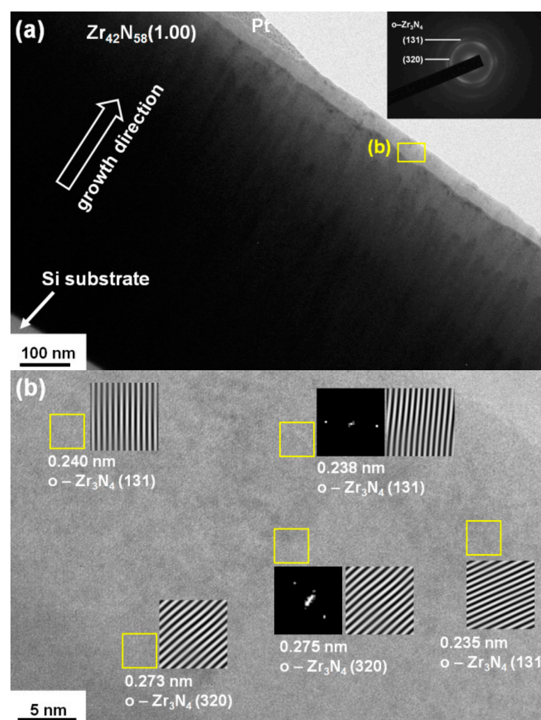

Figure 4. (**a**) Cross-sectional TEM image and SADP, and (**b**) high-resolution image of the $Zr_{42}N_{58}$(1.00) films.

3.2. Bonding Characteristics

The correlation between XRD and XPS analyses was applied to evaluate the mixture constitution of ZrN and Zr_3N_4 [26,38]. Figure 5 exhibits the XPS profiles of the Zr 3*d*, N 1*s*, and O 1*s* core levels of

the $Zr_{52}N_{48}$(0.50) films at sputter depths of 0 to 48 nm. The profiles at the free surface exhibited serious oxygen pollution because of a high affinity of Zr and O, whereas the profiles beneath the surface were not influenced by O. Figure 6 displays the curve-fitting results of the Zr 3*d* profiles at a sputter depth of 48 nm for the ZrN_x films. The XPS profiles comprised two doublets, representing Zr–N bonds for ZrN and Zr_3N_4 compounds. The binding energies of the two $3d_{5/2}$ signals of the $Zr_{52}N_{48}$(0.50) films were identified as 179.62 ± 0.04 and 181.59 ± 0.03 eV at depths of 8–48 nm for Zr–N in ZrN and Zr_3N_4, respectively. The intensity ratio of ZrN:Zr_3N_4 was 67:33. In our previous study [33], the Zr–N bonds for ZrN and Zr_3N_4 compounds of the $Zr_{60}N_{40}$(0.40) films were identified as 179.55 and 181.39 eV, respectively. The N profiles of the $Zr_{52}N_{48}$(0.50) films at depths of 8–48 nm were fitted with two signals with binding energies of 397.16 ± 0.01 and 396.31 ± 0.02 eV, representing N–Zr bonds for ZrN and Zr_3N_4 compounds, respectively. Prieto et al., [24] reported the N 1*s* values to be 397.3 and 396.4 eV for ZrN and Zr_3N_4, respectively. Furthermore, Prieto et al., [24] concluded that the Zr 3*d* and N 1*s* of Zr_3N_4 shifted in opposite directions with respect to those of ZrN, which resulted in an increase of the binding-energy deviation of N 1*s*, Zr 3*d* and the Zr_3N_4 becoming an insulator.

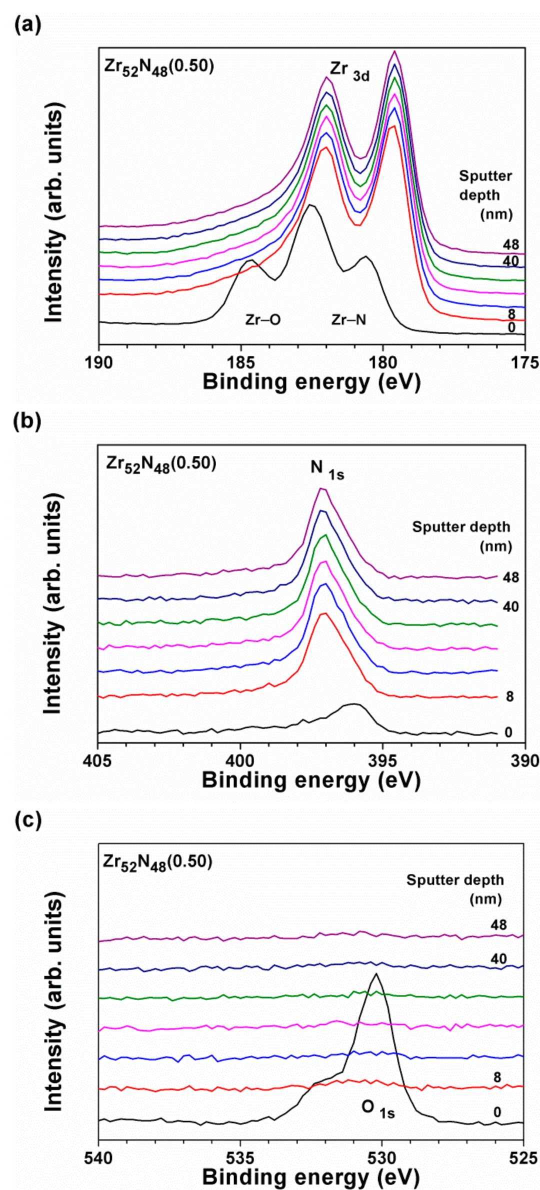

Figure 5. X-ray photoelectron spectroscope (XPS) profiles of the (**a**) Zr 3*d*, (**b**) N 1*s*, and (**c**) O 1*s* core levels of the $Zr_{52}N_{48}$(0.50) films at depths of 0 to 48 nm (sputter rate = 8 nm/min for SiO_2).

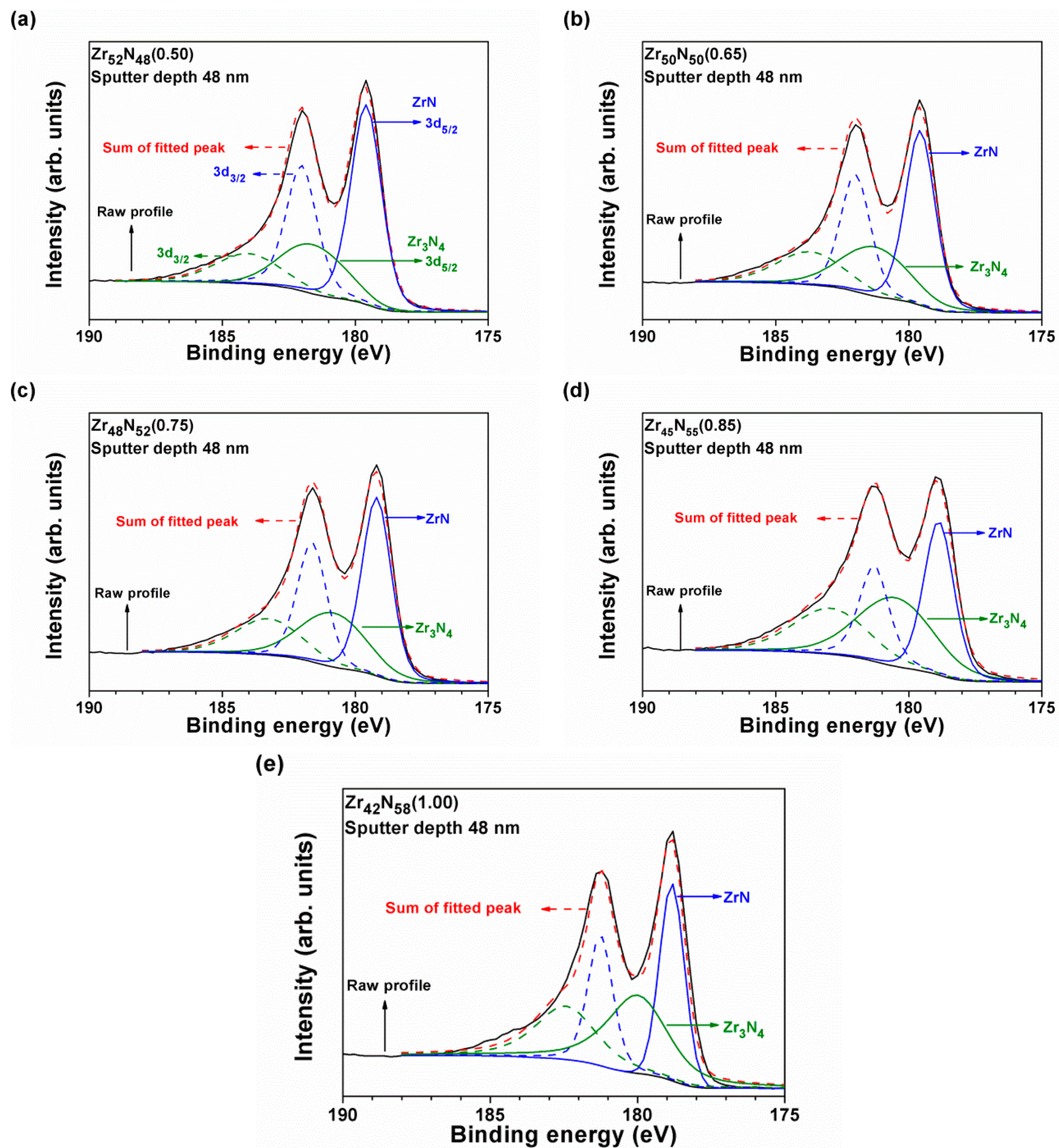

Figure 6. Curve fitting of the Zr 3*d* signals of (**a**) $Zr_{52}N_{48}$(0.50), (**b**) $Zr_{50}N_{50}$(0.65), (**c**) $Zr_{48}N_{52}$(0.75), (**d**) $Zr_{45}N_{55}$(0.85), and (**e**) $Zr_{42}N_{58}$(1.00) films at depths of 48 nm.

Figure 7 exhibits the XPS profiles of the Zr 3*d* and N 1*s* core levels of the ZrN_x films at a sputter depth of 48 nm. Both the Zr 3*d* and N 1*s* binding energies shifted towards lower levels with increasing N_2 flow ratios. Increasing the N_2 flow ratio to 1.00 decreased the $3d_{5/2}$ signal values of Zr–N bonds to 178.82 ± 0.02 and 180.06 ± 0.04 eV for ZrN and Zr_3N_4 compounds, respectively. Previously reported Zr $3d_{5/2}$ values of Zr–N bonds for ZrN_x were 178.8–179.8 eV [39–42], whereas those of Zr–N bonds for ZrN_{1+x} were 180.3–181.0 eV [40,41]. Table 2 lists the intensity ratios of the two $3d_{5/2}$ signals in the form ZrN:Zr_3N_4. The ratio of Zr–N bonds in the Zr_3N_4 compound increased with increasing N content in the ZrN_x films, which is an accordance with the observation on phase change by XRD. The ZrN_x films fabricated with an *f* value higher than 0.85 exhibited Zr_3N_4-dominant bonding structures.

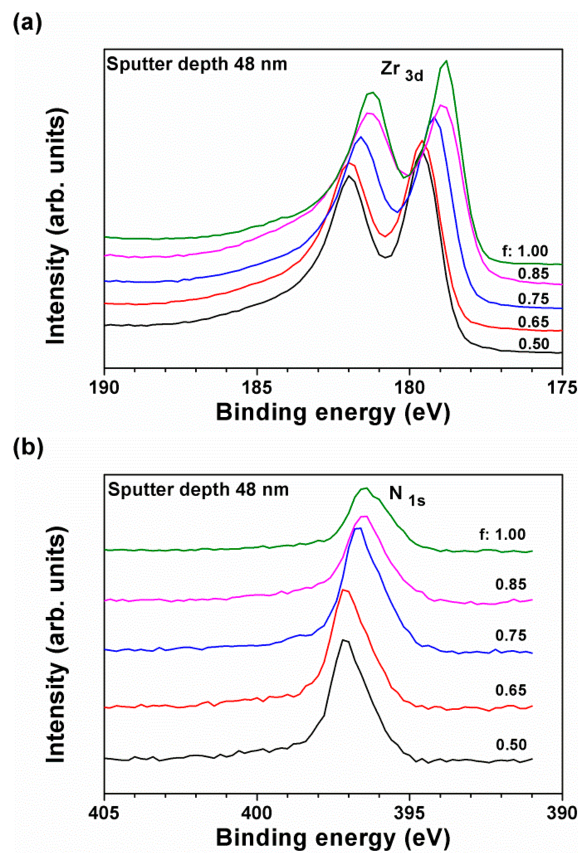

Figure 7. XPS profiles of the (**a**) Zr 3*d* and (**b**) N 1*s* core levels of the ZrN_x films (f = 0.50–1.00) at a sputter depth of 48 nm.

Table 2. XPS binding energies and intensity ratios of XRD reflections of the ZrN*x* films.

Sample	Zr $3d_{5/2}$ (eV) Zr–N(ZrN)	Zr–N(Zr_3N_4)	Intensity Ratio (XPS) ZrN:Zr_3N_4	Intensity Ratio (XRD) ZrN(111):Zr_3N_4(320)
$Zr_{60}N_{40}$(0.40)	179.55 ± 0.06	181.39 ± 0.05	80:20	100:0
$Zr_{52}N_{48}$(0.50)	179.62 ± 0.04	181.59 ± 0.03	67:33	54:46
$Zr_{50}N_{50}$(0.65)	179.59 ± 0.04	181.29 ± 0.04	59:41	49:51
$Zr_{48}N_{52}$(0.75)	179.14 ± 0.03	180.74 ± 0.05	56:44	44:56
$Zr_{45}N_{55}$(0.85)	178.84 ± 0.06	180.42 ± 0.04	48:52	37:63
$Zr_{42}N_{58}$(1.00)	178.82 ± 0.02	180.06 ± 0.04	44:56	33:67

3.3. Mechanical Properties

Table 3 shows the mechanical properties of ZrN_x films. The ZrN_x films prepared with f levels of 0.50–1.00 exhibited insignificant variations in hardness (18.3–19.0 GPa) and Young's modulus (210–234 GPa), although the residual stress ranged from −0.2 to −1.2 GPa. The $Zr_{45}N_{55}$(0.85) films exhibited an underestimated hardness of 17.3 GPa, which was attributed to the substrate effect because the indentation depth was 50 nm and the films possessed a low thickness of 348 nm (Table 1), which did not follow the 1/10 rule for accurate examination [43]. Figure 8 displays a representative curve of displacement against load in the nanoindentation test. The $Zr_{60}N_{40}$(0.40) films with a crystalline ZrN phase and a thickness of 820 nm exhibited a hardness of 21.0 GPa and a Young's modulus of 248 GPa, using an indentation depth of 80 nm accompanied with a residual stress of −0.9 GPa [30]. Qi et al., [5] reported that the hardness values of magnetron-sputtered ZrN films increased from 19.74 to 34.11 GPa as the negative bias voltage changed from 0 to 100 V, resulting in an increase in compressive stress from 0.50 to 4.24 GPa and a decrease in grain size from 43.4 to 11.6 nm. Further increasing the bias voltage decreased the hardness because of the inverse Hall–Petch effect as the grain size was <10 nm.

In the work of Mae et al. [44], the ZrN films fabricated without bias application exhibited a stress ranging from −1 to −2.5 GPa, corresponding to a hardness level of 16–25 GPa depending on the N_2 flow rate in the reactive gas. A higher N_2 flow rate produced films with a lower hardness and stress. In the works of Abadias et al. [45], magnetron-sputtered ZrN films exhibited a hardness of 21.0 GPa. Previous studies indicated that the hardness of o-Zr_3N_4 was similar to that of ZrN [25,46]. In summary, the hardness values of crystalline ZrN films were related to their stressed conditions. The mechanical properties of $ZrN_x(f)$ films (f = 0.50–1.00) were dominated by the o-Zr_3N_4 phase in a nanocrystalline form accompanied with a low compressive stress level; therefore, the Young's modulus exhibited a slight decreasing trend and the hardness maintained a constant level as the f value increased. Moreover, the evaluation of thin film mechanical properties by nanoindentation technique was affected by the surface roughness [47]. Surface roughness reduced averages and enlarged deviations of nanoindentation hardness and Young's modulus. All the ZrN_x films exhibited a low average surface roughness of 0.7–1.2 nm (Table 3); therefore, the error in the determination of mechanical properties was negligible.

Table 3. Mechanical properties and surface roughness values of ZrN_x films.

Sample	Hardness (GPa)	Young's Modulus (GPa)	Stress (GPa)	Roughness (nm)
$Zr_{60}N_{40}$(0.40)	21.0 ± 0.3	248 ± 6	−0.9 ± 0.2	1.0 ± 0.0
$Zr_{52}N_{48}$(0.50)	18.9 ± 1.0	228 ± 10	−0.6 ± 0.1	1.2 ± 0.0
$Zr_{50}N_{50}$(0.65)	19.0 ± 0.5	234 ± 6	−0.2 ± 0.2	1.0 ± 0.1
$Zr_{48}N_{52}$(0.75)	18.8 ± 0.9	228 ± 5	−0.5 ± 0.1	0.7 ± 0.0
$Zr_{45}N_{55}$(0.85)	17.3 ± 0.4	211 ± 3	−0.7 ± 0.2	0.8 ± 0.1
$Zr_{42}N_{58}$(1.00)	18.3 ± 0.9	210 ± 5	−1.2 ± 0.1	1.0 ± 0.0

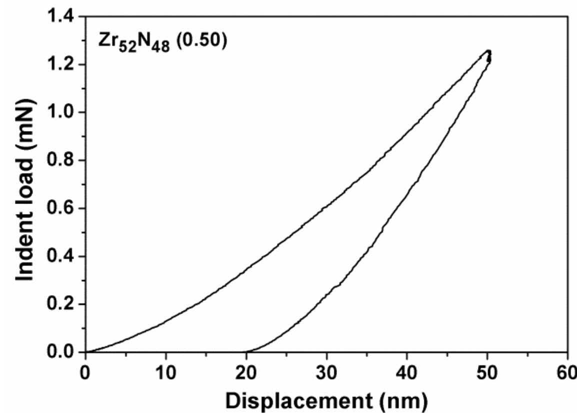

Figure 8. Typical load-displacement curve of nanoindentation tests.

4. Conclusions

$ZrN_x(f)$ films with the stoichiometric variable x ranging from 0.67 to 1.38 were fabricated on Si substrates through reactive direct current magnetron sputtering by varying the nitrogen flow ratio f from 0.4 to 1.0. As nitrogen flow ratio increased, the crystalline structure of the investigated ZrN_x films varied from a cubic ZrN phase for $Zr_{60}N_{40}$(0.40) films to a mixed nanostructure of cubic ZrN and orthorhombic Zr_3N_4 phases for $Zr_{52}N_{48}$(0.50), $Zr_{50}N_{50}$(0.65), and $Zr_{48}N_{52}$(0.75) films, and to a Zr_3N_4-dominated nanostructure for $Zr_{45}N_{55}$(0.85) and $Zr_{42}N_{58}$(1.00) films. The variation in phase from ZrN to Zr_3N_4-dominated, analyzed by X-ray diffraction, was consistent with the alteration in bonding characteristics examined by X-ray photoelectron spectroscopy. The hardness and Young's modulus of $Zr_{60}N_{40}$(0.40) films were 21.0 and 248 GPa, respectively. The hardness levels of ZrN_x (x = 0.92–1.38) films were 18.3 to 19.0 GPa with a negligible deviation, and the Young's modulus of the films decreased slightly from 234 to 210 GPa, which were attributed to the formation of the nanocrystalline

o-Zr_3N_4 constitution and the films maintained at a low compressive residual stress level ranged from −0.2 to −1.2 GPa and a low surface roughness of 0.7–1.2 nm.

Author Contributions: Conceptualization, Y.-I.C.; funding acquisition, Y.-I.C.; investigation, Y.-E.K.; project administration, Y.-I.C.; validation, Y.-E.K. and Y.-I.C.; writing—original draft, Y.-E.K.; writing—review and editing, Y.-I.C. All authors have read and agreed to the published version of the manuscript.

Funding: This research was funded by the Ministry of Science and Technology, Taiwan, Grant Nos. 106-2221-E-019-022-MY3 and 107-2813-C-019-019-E.

Acknowledgments: The authors thank Ching-Wen Tsai at the Instrumentation Center at the National Tsing Hua University for technical support with the XPS analyses. The authors thank Su-Yueh Tsai at the Instrumentation Center at the National Tsing Hua University for technical support with the FE-EPMA analyses.

Conflicts of Interest: The authors declare no conflicts of interest.

References

1. Perry, A.J.; Georgson, M.; Sproul, W.D. Variations in the reflectance of TiN, ZrN and HfN. *Thin Solid Films* **1988**, *157*, 255–265. [CrossRef]
2. Budke, E.; Krempel-Hesse, J.; Maidhof, H.; Schüssler, H. Decorative hard coatings with improved corrosion resistance. *Surf. Coat. Technol.* **1999**, *112*, 108–113. [CrossRef]
3. Chou, W.J.; Yu, G.P.; Huang, J.H. Bias effect of ion-plated zirconium nitride film on Si(100). *Thin Solid Films* **2002**, *405*, 162–169. [CrossRef]
4. Purandare, Y.P.; Ehiasarian, A.P.; Hovsepian, P.E. Structure and properties of ZrN coatings deposited by high power impulse magnetron sputtering technology. *J. Vac. Sci. Technol. A* **2011**, *29*, 011004. [CrossRef]
5. Qi, Z.B.; Sun, P.; Zhu, F.P.; Wang, Z.C.; Peng, D.L.; Wu, C.H. The inverse Hall–Petch effect in nanocrystalline ZrN coatings. *Surf. Coat. Technol.* **2011**, *205*, 3692–3697. [CrossRef]
6. Chang, L.C.; Chang, C.Y.; Chen, Y.I.; Kao, H.L. Mechanical properties and oxidation behavior of ZrN_x thin films fabricated through high-power impulse magnetron sputtering deposition. *J. Vac. Sci. Technol. A* **2016**, *34*, 02D107. [CrossRef]
7. Chou, W.J.; Yu, G.P.; Huang, J.H. Corrosion resistance of ZrN films on AISI 304 stainless steel substrate. *Surf. Coat. Technol.* **2003**, *167*, 59–67. [CrossRef]
8. Xin, Y.; Liu, C.; Huo, K.; Tang, G.; Tian, X.; Chu, P.K. Corrosion behavior of ZrN/Zr coated biomedical AZ91 magnesium alloy. *Surf. Coat. Technol.* **2009**, *203*, 2554–2557. [CrossRef]
9. Roman, D.; Bernardi, J.; Amorim, C.; Souza, F.; Spinelli, A.; Giacomelli, C.; Figueroa, C.A.; Baumvol, I.J.R.; Basso, R.L.O. Effect of deposition temperature on microstructure and corrosion resistance of ZrN thin films deposited by DC reactive magnetron sputtering. *Mater. Chem. Phys.* **2011**, *130*, 147–153. [CrossRef]
10. Hu, C.; Guo, K.; Li, Y.; Gu, Z.; Quan, J.; Zhang, S.; Zheng, W. Optical coatings of durability based on transition metal nitrides. *Thin Solid Films* **2019**, *688*, 137339. [CrossRef]
11. Huang, J.H.; Lau, K.W.; Yu, G.P. Effect of nitrogen flow rate on structure and properties of nanocrystalline TiN thin films produced by unbalanced magnetron sputtering. *Surf. Coat. Technol.* **2005**, *191*, 17–24. [CrossRef]
12. Singh, A.; Kuppusami, P.; Khan, S.; Sudha, C.; Thirumurugesan, R.; Ramaseshan, R.; Divakar, R.; Mohandas, E.; Dash, S. Influence of nitrogen flow rate on microstructural and nanomechanical properties of Zr–N thin films prepared by pulsed DC magnetron sputtering. *Appl. Surf. Sci.* **2013**, *280*, 117–123. [CrossRef]
13. Gu, Z.; Hu, C.; Huang, H.; Zhang, S.; Fan, X.; Wang, X.; Zheng, W. Identification and thermodynamic mechanism of the phase transition in hafnium nitride films. *Acta Mater.* **2015**, *90*, 59–68. [CrossRef]
14. Balasubramanian, K.; Khare, S.V.; Gall, D. Energetics of point defects in rocksalt structure transition metal nitrides: Thermodynamic reasons for deviations from stoichiometry. *Acta Mater.* **2018**, *159*, 77–88. [CrossRef]
15. Kroll, P. Hafnium nitride with thorium phosphide structure: Physical properties and an assessment of the Hf-N, Zr-N, and Ti-N phase diagrams at high pressures and temperatures. *Phys. Rev. Lett.* **2003**, *90*, 125501. [CrossRef] [PubMed]
16. Signore, M.A.; Valerini, D.; Tapfer, L.; Caretto, G.; Rizzo, A. Zirconium nitride films deposited in (Ar + N_2 + H_2) sputtering atmosphere: Optical, structural, and electrical properties. *J. Vac. Sci. Technol. A* **2011**, *29*, 061507. [CrossRef]
17. Lerch, M.; Füglein, E.; Wrba, J. Synthesis, Crystal structure, and high temperature behavior of Zr_3N_4. *Z. Anorg. Allg. Chem.* **1996**, *622*, 367–372. [CrossRef]

18. Takeyama, M.B.; Sato, M.; Noya, A. Thermally stable ZrN/Zr_3N_4 bilayered barrier system for through-Si-via process. *Jpn. J. Appl. Phys.* **2015**, *54*, 05EE02. [CrossRef]
19. Zerr, A.; Miehe, G.; Riedel, R. Synthesis of cubic zirconium and hafnium nitride having Th_3P_4 structure. *Nat. Mater.* **2003**, *2*, 185–189. [CrossRef]
20. Dzivenko, D.A.; Zerr, A.; Boehler, R.; Riedel, R. Equation of state of cubic hafnium(IV) nitride having Th_3P_4-type structure. *Solid State Commun.* **2006**, *139*, 255–258. [CrossRef]
21. Chihi, T.; Fatmi, M.; Ghebouli, B.; Guemmaz, M. Theoretical prediction of the structural, elastic, electronic and optical properties of Zr_3N_4 and Hf_3N_4 compounds. *Solid State Sci.* **2011**, *13*, 1414–1419. [CrossRef]
22. Zhang, J.D.; Yang, K. Theoretical study of the thermodynamic properties of cubic Zr_3N_4 and Hf_3N_4 under high pressures. *J. Alloy. Compd.* **2014**, *608*, 90–94. [CrossRef]
23. Mattesini, M.; Ahuja, R.; Johansson, B. Cubic Hf_3N_4 and Zr_3N_4: A class of hard materials. *Phys. Rev. B* **2003**, *68*, 184108. [CrossRef]
24. Prieto, P.; Galán, L.; Sanz, J.M. Electronic structure of insulating zirconium nitride. *Phys. Rev. B* **1993**, *47*, 1613–1615. [CrossRef] [PubMed]
25. Chhowalla, M.; Unalan, H.E. Thin films of hard cubic Zr_3N_4 stabilized by stress. *Nat. Mater.* **2005**, *4*, 317–322. [CrossRef] [PubMed]
26. Sui, Y.; Liu, J.; Liu, B.; Wang, L.; Yao, B. Influence of flow ratio of N_2 to (N_2+Ar) mixture on the structure and properties of zirconium nitride films prepared by radio frequency magnetron sputtering. *J. Mater. Res.* **2009**, *24*, 3206–3212. [CrossRef]
27. Meng, Q.N.; Wen, M.; Qu, C.Q.; Hu, C.Q.; Zheng, W.T. Preferred orientation, phase transition and hardness for sputtered zirconium nitride films grown at different substrate biases. *Surf. Coat. Technol.* **2011**, *205*, 2865–2870. [CrossRef]
28. Norouzian, S.; Larijani, M.M.; Afzalzadeh, R. Effect of nitrogen flow ratio on structure and properties of zirconium nitride films on Si(100) prepared by ion beam sputtering. *Bull. Mater. Sci.* **2012**, *35*, 885–887. [CrossRef]
29. Ke, Y.E.; Chen, Y.I. Mechanical properties, bonding characteristics, and thermal stability of magnetron-sputtered HfNx films. *Surf. Coat. Technol.* **2020**, *388*, 125575. [CrossRef]
30. Oliver, W.C.; Pharr, G.M. An improved technique for determining hardness and elastic modulus using load and displacement sensing indentation experiments. *J. Mater. Res.* **1992**, *7*, 1564–1583. [CrossRef]
31. Janssen, G.C.A.M.; Abdalla, M.M.; van Keulen, F.; Pujada, B.R.; van Venrooy, B. Celebrating the 100th anniversary of the Stoney equation for film stress: Developments from polycrystalline steel strips to single crystal silicon wafers. *Thin Solid Films* **2009**, *517*, 1858–1867. [CrossRef]
32. Chen, Y.I.; Chang, S.C.; Chang, L.C. Oxidation resistance and mechanical properties of Zr–Si–N coatings with cyclic gradient concentration. *Surf. Coat. Technol.* **2017**, *320*, 168–173. [CrossRef]
33. Chang, L.C.; Zheng, Y.Z.; Chen, Y.I.; Chang, S.C.; Liu, B.W. Bonding characteristics and chemical inertness of Zr–Si–N coatings with a high Si content in glass molding. *Coatings* **2018**, *8*, 181. [CrossRef]
34. Ruan, J.L.; Lii, D.F.; Lu, H.H.; Chen, J.S.; Huang, J.L. Microstructural and electrical characteristics of reactively sputtered ZrN*x* thin films. *J. Alloy. Compd.* **2009**, *478*, 671–675. [CrossRef]
35. Ramana, J.V.; Kumar, S.; David, C.; Ray, A.K.; Raju, V.S. Characterisation of zirconium nitride coatings prepared by DC magnetron sputtering. *Mater. Lett.* **2000**, *43*, 73–76. [CrossRef]
36. Berg, S.; Nyberg, T. Fundamental understanding and modeling of reactive sputtering processes. *Thin Solid Films* **2005**, *476*, 215–230. [CrossRef]
37. Huang, J.H.; Ho, C.H.; Yu, G.P. Effect of nitrogen flow rate on the structure and mechanical properties of ZrN thin films on Si(1 0 0) and stainless steel substrates. *Mater. Chem. Phys.* **2007**, *102*, 31–38. [CrossRef]
38. Sui, Y.R.; Xu, Y.; Yao, B.; Xiao, L.; Liu, B. Preparation, characterization and properties of N-rich Zr–N thin film with Th_3P_4 structure. *Appl. Surf. Sci.* **2009**, *255*, 6355–6358. [CrossRef]
39. Höchst, H.; Bringans, R.D.; Steiner, P.; Wolf, T. Photoemission study of the electronic structure of stoichiometric and substoichiometric TiN and ZrN. *Phys. Rev. B* **1982**, *25*, 7183–7191. [CrossRef]
40. Netterfield, R.P.; Martin, P.J.; McKenzie, D.R. Properties of ZrNx prepared by ion-assisted deposition. *J. Mater. Sci. Lett.* **1990**, *9*, 972–974. [CrossRef]
41. Bertóti, I. Characterization of nitride coatings by XPS. *Surf. Coat. Technol.* **2002**, *151–152*, 194–203. [CrossRef]

42. Carvalho, P.; Chappé, J.M.; Cunha, L.; Lanceros-Méndez, S.; Alpuim, P.; Vaz, F.; Alves, E.; Rousselot, C.; Espinós, J.P.; González-Elipe, A.R. Influence of the chemical and electronic structure on the electrical behavior of zirconium oxynitride films. *J. Appl. Phys.* **2008**, *103*, 104907. [CrossRef]
43. Saha, R.; Nix, W.D. Effects of the substrate on the determination of thin film mechanical properties by nanoindentation. *Acta Mater.* **2002**, *50*, 23–38. [CrossRef]
44. Mae, T.; Nose, M.; Zhou, M.; Nagae, T.; Shimamura, K. The effects of Si addition on the structure and mechanical properties of ZrN thin films deposited by an r.f. reactive sputtering method. *Surf. Coat. Technol.* **2001**, *142–144*, 954–958. [CrossRef]
45. Abadias, G.; Uglov, V.V.; Saladukhin, I.A.; Zlotski, S.V.; Tolmachova, G.; Dub, S.N.; Janse van Vuuren, A. Growth, structural and mechanical properties of magnetron-sputtered ZrN/SiNx nanolaminated coatings. *Surf. Coat. Technol.* **2016**, *308*, 158–167. [CrossRef]
46. Ushakov, S.V.; Navrotsky, A.; Hong, Q.J.; van de Walle, A. Carbides and nitrides of zirconium and hafnium. *Materials* **2019**, *12*, 2728. [CrossRef]
47. Qasmi, M.; Delobelle, P. Influence of the average roughness Rms on the precision of the Young's modulus and hardness determination using nanoindentation technique with a Berkovich indenter. *Surf. Coat. Technol.* **2006**, *201*, 1191–1199. [CrossRef]

© 2020 by the authors. Licensee MDPI, Basel, Switzerland. This article is an open access article distributed under the terms and conditions of the Creative Commons Attribution (CC BY) license (http://creativecommons.org/licenses/by/4.0/).